Hybrid dielectric light trapping designs for thin-film CdZnTe/Si tandem cells

H. Chung,[1] C. Zhou,[1] X. T. Tee,[1] K.-Y. Jung,[2] and P. Bermel[1,*]

[1]*School of Electrical & Computer Engineering, Purdue University, West Lafayette, Indiana, USA*

[2]*Department of Electronic Engineering, Hanyang University, Seoul, South Korea*

*pbermel@purdue.edu

Abstract: Tandem solar cells consisting of high bandgap cadmium telluride alloys atop crystalline silicon have potential for high efficiencies exceeding the Shockley-Queisser limit. However, experimental results have fallen well below this goal significantly because of non-ideal current matching and light trapping. In this work, we simulate cadmium zinc telluride (CZT) and crystalline silicon (c-Si) tandems as an exemplary system to show the role that a hybrid light trapping and bandgap engineering approach can play in improving performance and lowering materials costs for tandem solar cells incorporating crystalline silicon. This work consists of two steps. First, we optimize absorption in the crystalline silicon layer with front pyramidal texturing and asymmetric dielectric back gratings, which results in 121% absorption enhancement from a planar structure. Then, using this pre-optimized light trapping scheme, we model the dispersion of the $Cd_xZn_{1-x}Te$ alloys, and then adjust the bandgap to realize the best current matching for a range of CZT thicknesses. Using experimental parameters, the corresponding maximum efficiency is predicted to be 16.08 % for a total tandem cell thickness of only 2.2 μm.

© 2016 Optical Society of America

OCIS codes: (350.4238) Nanophotonics and photonic crystals; (350.6050) Solar energy.

References and links

1. W. Shockley and H. J. Queisser, "Detailed balance limit of efficiency of p-n junction solar cells," J. Appl. Phys. **32**, 510–519 (1961).
2. M. A. Green, K. Emery, Y. Hishikawa, W. Warta, and E. D. Dunlop, "Solar cell efficiency tables (version 45)," Prog. Photovolt. Res. Appl. **23**, 1–9 (2015).
3. A. De Vos, "Detailed balance limit of the efficiency of tandem solar cells," J, of Phys. D: Appl. Phys. **13**, 839 (1980).
4. D. Staebler and C. Wronski, "Reversible conductivity changes in discharge-produced amorphous si," Appl. Phys. Lett. **31**, 292–294 (1977).
5. H. Zhou, Q. Chen, G. Li, S. Luo, T.-b. Song, H.-S. Duan, Z. Hong, J. You, Y. Liu, and Y. Yang, "Interface engineering of highly efficient perovskite solar cells," Science **345**, 542–546 (2014).
6. S. Albrecht, M. Saliba, J. P. C. Baena, F. Lang, L. Kegelmann, M. Mews, L. Steier, A. Abate, J. Rappich, L. Korte, R. Schlatmann, M. Nazeeruddin, A. Hagfeldt, M. Grätzel, and B. Rech, "Monolithic perovskite/silicon-heterojunction tandem solar cells processed at low temperature," Energy & Environmental Science (2016).
7. N. Chander, A. Khan, P. Chandrasekhar, E. Thouti, S. K. Swami, V. Dutta, and V. K. Komarala, "Reduced ultraviolet light induced degradation and enhanced light harvesting using YVO4: Eu3+ down-shifting nano-phosphor layer in organometal halide perovskite solar cells," Appl. Phys. Lett. **105**, 033904 (2014).
8. J. Yang, B. D. Siempelkamp, D. Liu, and T. L. Kelly, "Investigation of CH3NH3PbI3 degradation rates and mechanisms in controlled humidity environments using in situ techniques," ACS Nano **9**, 1955–1963 (2015).

#262116 Received 1 Apr 2016; revised 9 May 2016; accepted 10 May 2016; published 20 May 2016
© 2016 OSA

9. M. Carmody, S. Mallick, J. Margetis, R. Kodama, T. Biegala, D. Xu, P. Bechmann, J. Garland, and S. Sivananthan, "Single-crystal II-VI on si single-junction and tandem solar cells," Appl. Phys. Lett. **96**, 153502 (2010).
10. D. Xu, T. Biegala, M. Carmody, J. W. Garland, C. Grein, and S. Sivananthan, "Proposed monolithic triple-junction solar cell structures with the potential for ultrahigh efficiencies using II–VI alloys and silicon substrates," Appl. Phys. Lett. **96**, 073508 (2010).
11. J. Garland, T. Biegala, M. Carmody, C. Gilmore, and S. Sivananthan, "Next-generation multijunction solar cells: The promise of II-VI materials," J. Appl. Phys. **109**, 102423 (2011).
12. M. Gloeckler, A. Fahrenbruch, and J. Sites, "Numerical modeling of CIGS and CdTe solar cells: setting the baseline," in Proceedings of IEEE Conference on Photovoltaic Energy Conversion (IEEE, 2003), pp. 491–494.
13. K. Sato and S. Adachi, "Optical properties of ZnTe," J. Appl. Phys. **73**, 926–931 (1993).
14. C. Zhou, H. Chung, X. Wang, and P. Bermel, "Design of CdZnTe and crystalline silicon tandem junction solar cells," IEEE J. Photovolt. **6**, 301–308 (2016).
15. A. Hübner, A. G. Aberle, and R. Hezel, "Novel cost-effective bifacial silicon solar cells with 19.4% front and 18.1% rear efficiency," Appl. Phys. Lett. **70**, 1008–1010 (1997).
16. R. Asadpour, R. V. Chavali, M. R. Khan, and M. A. Alam, "Bifacial si heterojunction-perovskite organic-inorganic tandem to produce highly efficient (ηt* 33%) solar cell," Appl. Phys. Lett. **106**, 243902 (2015).
17. A. Tavlove and S. C. Hagness, "Computational electrodynamics: the finite-difference time-domain method," Artech House, Norwood, MA **2062** (1995).
18. G. Jellison Jr and F. Modine, "Parameterization of the optical functions of amorphous materials in the interband region," Appl. Phys. Lett. **69**, 371–373 (1996).
19. J. N. Munday and H. A. Atwater, "Large integrated absorption enhancement in plasmonic solar cells by combining metallic gratings and antireflection coatings," Nano Lett. **11**, 2195–2201 (2010).
20. D. Madzharov, R. Dewan, and D. Knipp, "Influence of front and back grating on light trapping in microcrystalline thin-film silicon solar cells," Opt. Express **19**, A95–A107 (2011).
21. A. Chutinan, N. P. Kherani, and S. Zukotynski, "High-efficiency photonic crystal solar cell architecture," Opt. Express **17**, 8871–8878 (2009).
22. H. Chung, K.-Y. Jung, and P. Bermel, "Flexible flux plane simulations of parasitic absorption in nanoplasmonic thin-film silicon solar cells," Opt. Mat. Express **5**, 2054–2068 (2015).
23. A. Sadao and K. Toshifumi, "Optical constants of $Zn_{1-x}Cd_xTe$ ternary alloys: Experiment and modeling," Jpn. J. Appl. Phys **32**, 3496–3501 (1993).
24. O. Castaing, J. Benhlal, and R. Granger, "An attempt to model the dielectric function in II-VI ternary compounds and," The European Phys. J. B-Condensed Matter and Complex Systems **7**, 563–572 (1999).
25. A. Parikh, J. Li, J. Chen, S. Marsilac, and R. Collins, "Optical analysis of II–VI alloys and structures for tandem PV," in Proceedings of IEEE Conference on Photovoltaic Specialist (IEEE, 2008), pp. 1–5.
26. S.-G. Ha, J. Cho, J. Choi, H. Kim, and K.-Y. Jung, "FDTD dispersive modeling of human tissues based on quadratic complex rational function," IEEE Trans. Antennas Propag. **61**, 996–999 (2013).
27. R. Collins, A. Ferlauto, G. Ferreira, C. Chen, J. Koh, R. Koval, Y. Lee, J. Pearce, and C. Wronski, "Evolution of microstructure and phase in amorphous, protocrystalline, and microcrystalline silicon studied by real time spectroscopic ellipsometry," Sol. Energy Mater. Sol. Cells **78**, 143–180 (2003).
28. E. D. Palik, *Handbook of Optical Constants of Solids: Index*, vol. 3 (Access Online via Elsevier, 1998).
29. H. Chung, K.-Y. Jung, X. Tee, and P. Bermel, "Time domain simulation of tandem silicon solar cells with optimal textured light trapping enabled by the quadratic complex rational function," Opt. Express **22**, A818–A832 (2014).
30. J. Cho, S.-G. Ha, Y. B. Park, H. Kim, and K.-Y. Jung, "On the numerical stability of finite-difference time-domain for wave propagation in dispersive media using quadratic complex rational function," Electromagnetics **34**, 625–632 (2014).
31. Y. Jiang, M. A. Green, R. Sheng, and A. Ho-Baillie, "Room temperature optical properties of organic–inorganic lead halide perovskites," Sol. Energy Mater. and Sol. Cells **137**, 253–257 (2015).
32. H. Duan, X. Chen, Y. Huang, X. Zhou, L. Sun, and W. Lu, "Composition-dependent electronic properties, optical transitions, and anionic relaxations of cd 1- x zn x te alloys from first principles," Phys. Review B **76**, 035209 (2007).
33. N. Korozlu, K. Colakoglu, and E. Deligoz, "Structural, electronic, elastic and optical properties of cdxzn1- xte mixed crystals," J. of Phys.: Condensed Matter **21**, 175406 (2009).
34. S. Johnson, S. Sen, W. Konkel, and M. Kalisher, "Optical techniques for composition measurement of bulk and thin-film cd1- yznyte," J. of Vacuum Science & Tech. B **9**, 1897–1901 (1991).
35. S. J. Orfanidis, *Electromagnetic Waves and Antennas* (Rutgers University, 2002).
36. A. W. Blakers, A. Wang, A. M. Milne, J. Zhao, and M. A. Green, "22.8% efficient silicon solar cell," Appl. Phys. Lett. **55**, 1363–1365 (1989).
37. D. Qi, N. Lu, H. Xu, B. Yang, C. Huang, M. Xu, L. Gao, Z. Wang, and L. Chi, "Simple approach to wafer-scale self-cleaning antireflective silicon surfaces," Langmuir **25**, 7769–7772 (2009).
38. G. Yue, L. Sivec, J. M. Owens, B. Yan, J. Yang, and S. Guha, "Optimization of back reflector for high efficiency hydrogenated nanocrystalline silicon solar cells," Appl. Phys. Lett. **95**, 263501 (2009).

#262116 Received 1 Apr 2016; revised 9 May 2016; accepted 10 May 2016; published 20 May 2016
© 2016 OSA

39. H. Sai, H. Fujiwara, M. Kondo, and Y. Kanamori, "Enhancement of light trapping in thin-film hydrogenated microcrystalline si solar cells using back reflectors with self-ordered dimple pattern," Appl. Phys. Lett. **93**, 143501–143501 (2008).
40. J. Eisenlohr, B. G. Lee, J. Benick, F. Feldmann, M. Drießen, N. Milenkovic, B. Bläsi, J. C. Goldschmidt, and M. Hermle, "Rear side sphere gratings for improved light trapping in crystalline silicon single junction and silicon-based tandem solar cells," Sol. Energy Mater. and Sol. Cells **142**, 60–65 (2015).
41. H. Tan, R. Santbergen, A. H. Smets, and M. Zeman, "Plasmonic light trapping in thin-film silicon solar cells with improved self-assembled silver nanoparticles," Nano Lett. **12**, 4070–4076 (2012).
42. H. Tan, L. Sivec, B. Yan, R. Santbergen, M. Zeman, and A. H. Smets, "Improved light trapping in microcrystalline silicon solar cells by plasmonic back reflector with broad angular scattering and low parasitic absorption," Appl. Phys. Lett. **102**, 153902 (2013).
43. J. Springer, A. Poruba, L. Müllerova, M. Vanecek, O. Kluth, and B. Rech, "Absorption loss at nanorough silver back reflector of thin-film silicon solar cells," J. Appl. Phys. **95**, 1427–1429 (2004).
44. J. Gjessing, E. S. Marstein, and A. Sudbø, "2d back-side diffraction grating for improved light trapping in thin silicon solar cells," Opt. Express **18**, 5481–5495 (2010).
45. S. Y. Nof, A. M. Weiner, and G. J. Cheng, *Laser and Photonic Systems: Design and Integration* (CRC Press, 2014).
46. M. Kroll, S. Fahr, C. Helgert, C. Rockstuhl, F. Lederer, and T. Pertsch, "Employing dielectric diffractive structures in solar cells–a numerical study," physica status solidi (a) **205**, 2777–2795 (2008).
47. H. Sai, H. Jia, and M. Kondo, "Impact of front and rear texture of thin-film microcrystalline silicon solar cells on their light trapping properties," J. of Appl. Phys. **108**, 044505 (2010).
48. H. Sai, K. Saito, N. Hozuki, and M. Kondo, "Relationship between the cell thickness and the optimum period of textured back reflectors in thin-film microcrystalline silicon solar cells," Appl. Phys. Lett. **102**, 053509 (2013).

1. Introduction

Solar energy is one of the important renewable sources of energy, currently dominated by crystalline silicon. However, its efficiency has plateaued around 25 % over the past 2 decades. This result is already close to the fundamental Shockley-Queisser limit of single junction efficiency (31 % under 1 sun illumination) [1]. One proven approach for transcending these limits uses multiple junctions [2]. Although double junction solar cells theoretically can have up to 42 % [3], stabilized efficiencies of commercialized micromorph silicon tandem cells have not been improved significantly from 12 % [2, 4].

Perovskite-based solar cells have recently garnered a great deal of attention as an alternative offering high efficiencies and low costs [5, 6], but material stability issues (e.g., light soaking, humidity exposure) have not been fully addressed yet [7, 8]. Another alternative, recently, cadmium zinc telluride (CZT) has recently been studied for its potential low manufacturing costs, long recombination lifetimes, and high stability [9–11]. Furthermore, the bandgap of CZT can be tuned from 1.5 eV up to 2.26 eV, the range required for a top junction material [12, 13]. Recent experiments demonstrated 17 % cell efficiency using CZT/Si tandem cells [9–11]. These can be considered to be a very promising initial result. A physics-based modeling also predicted that the CZT/Si tandem cells can have up to 34.1 % with appropriate junction designs [14]. Also, CZT/Si tandem cells can be potentially applied to a bifacial configuration which have been studied for both micromorph silicon tandem cells [15] and perovskite/silicon tandem cells [16], possibly without requiring much zinc alloying, since the cadmium telluride bandgap is close to that of the methylammonium lead iodide perovskite. Furthermore, this approach is not necessarily limited to zinc alloys, but could include other high bandgap ternary compounds, such as magnesium cadmium telluride.

In this work, we consider light trapping strategies to fill the gap between the experiments and theory for CZT/Si tandem cells. The nature of the adjustable bandgap of CZT was one of the advantage in tandem cell applications, but it also gives rise to a complicated current matching problem. Thus, in this work, we focus on developing light trapping schemes for the CZT/Si tandem cells, and studying current matching condition for an adjustable CZT bandgap. First, we develop a material model for CZT alloys and demonstrate its accuracy by comparing it with

#262116 Received 1 Apr 2016; revised 9 May 2016; accepted 10 May 2016; published 20 May 2016
© 2016 OSA

analytic solutions. Then, we explore light trapping strategies (front texturing and asymmetric dielectric gratings) to turn the wafer-based cells into ultra-thin film cells. Then, the optimized light trapping scheme will be combined with adjustable CZT bandgaps to achieve current matching conditions.

2. Material modeling

We begin our optical modeling by first considering a variety of cadmium telluride-based alloys (e.g., CdZnTe, CdMgTe and CdHgTe). We then incorporate these models into a study of light trapping schemes using the finite difference time domain (FDTD) method [17]. The FDTD method directly simulates Maxwell's equations over time and space, and is highly accurate. One advantage for calculating absorption spectra is that it can incorporate a broad range of frequencies in one simulation, given an appropriate time domain dispersion model of photovoltaic materials. However, most semiconductor materials do not simply follow the commonly used Drude-Lorentz model at visible wavelengths, because there are many optical transitions above the bandgap energy [18]. Due to the lack of time domain broadband dispersion models for many photovoltaic materials, several simulated works have not fully utilized the potential of the FDTD method. Rather, the need to constrain the total computation for many frequencies has often limited researchers to 2-D FDTD simulations [19, 20] or required simplified coupled mode analysis, which requires certain conditions on resonant modes to be valid [21]. In this work, we developed a highly efficient modeling approach for CZT alloys in the time domain. This allows us to calculate the entire frequency response in 2 simulations even over a range of 200 distinct frequencies. The other simulation challenge in photovoltaic simulations is calculating and integrating losses over a substantial photovoltaic volume without greatly slowing down the main FDTD calculation . The authors recently developed an efficient surface integration method in an arbitrary curved geometry for FDTD, which is called Flexible Flux Plane (FFP) [22]. Combining the FFP and the quadratic complex rational function (QCRF) approaches dramatically reduces the simulation time in FDTD, allowing us to optimize the complex 3-D structure of CZT/Si tandem cells with reasonable computational resources (64

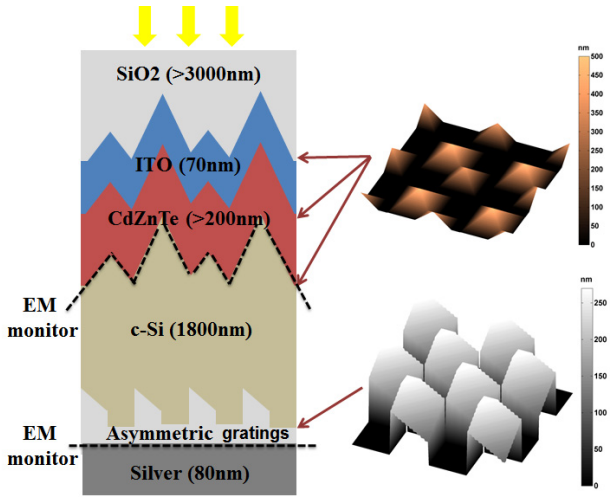

Fig. 1. Cross section of a CZT/Si tandem solar cell. It has a front periodic pyramidal texturing, conformally applied to ITO, CZT and c-Si. At the back reflector, an asymmetric grating is applied to enhance light absorption. The electromagnetic flux monitors were placed to calculate the top and bottom junction absorption.

#262116 Received 1 Apr 2016; revised 9 May 2016; accepted 10 May 2016; published 20 May 2016
© 2016 OSA

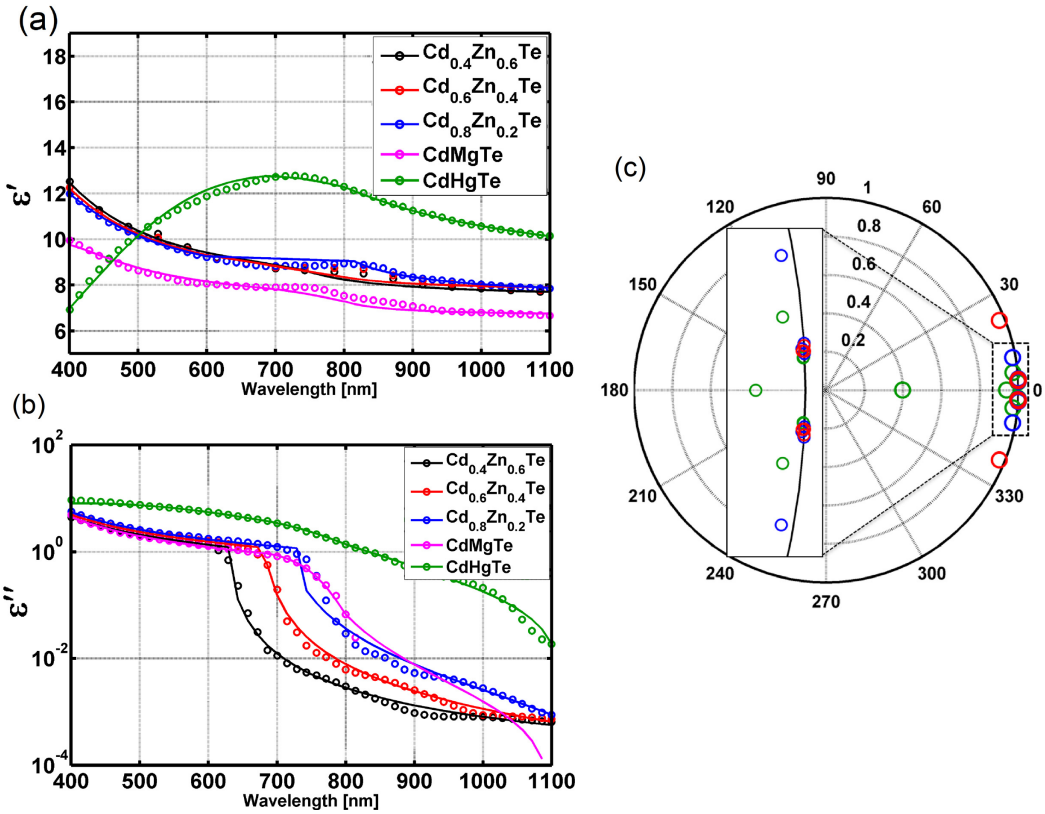

Fig. 2. (a) The QCRF model of the real part of permittivity of $Cd_xZn_{1-x}Te$, CdMgTe (1.6 eV) and CdHgTe (1.6 eV). The dots are the measurement data extracted from Refs. [23–25] and the lines are the QCRF modeling results. In this work, the QCRF method is applied to two different wavelength ranges, which were split near material band edges. (b) The QCRF modeling results on the imaginary part of permittivity of $Cd_xZn_{1-x}Te$, CdMgTe and CdHgTe. (c) Scatter plot of the von Neumann stability polynomial solution for the modeled CdTe alloys, which indicates the materials are unconditionally stable in FDTD.

cores in total). The schematic simulation structure of CZT/Si tandem cell is shown in Fig 1.

Modeling the optical properties of materials in CZT/Si tandem cells is performed using a recently developed general dispersion model known as the QCRF model [26]. For most dispersive materials (e.g., c-Si [27], silver [28]), we employed previously modeled QCRF data [29] and, in this work, $Cd_xZn_{(1-x)}Te$, CdMgTe and CdHgTe are modeled by two split QCRF coefficients over the wavelength range of 400—1100 nm, in which most useful solar photons can be found. Their numerical stability is validated by von Neumann analysis [30], and their accuracy is verified by 1-D FDTD simulation with a single layer dielectric slab.

As shown in Figs. 2(a) and 2(b), QCRF modeling has very good agreement with the spectroscopic elipsometry [31] measurement data of CdTe alloys collected from other Refs. [23–25,32–34]. In particular, the imaginary part of the dielectric function of $Cd_xZn_{(1-x)}Te$ varies rapidly near the band edge, so we model the CZT material with two frequency ranges, split near the bandgap. We modeled various alloy compositions of $Cd_xZn_{(1-x)}Te$ from $x = 0$ to $x = 1$ and a representative samples are presented in Fig. 2(a) and 2(b). The modeled fittings have root mean square (RMS) errors ranging from 1.85 to 2.64%. To validate the numerical stability of the modeled dispersions, von Neumann stability analysis was applied to calculate

#262116 Received 1 Apr 2016; revised 9 May 2016; accepted 10 May 2016; published 20 May 2016
© 2016 OSA

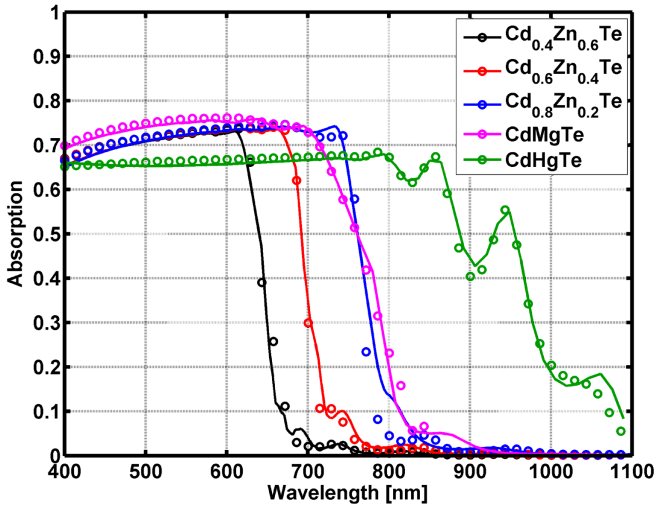

Fig. 3. Absorption profile in the 1000-nm-thick dielectric slab of CdTe alloys. The circular symbols indicate absorption spectrum obtained analytically [29], using measurements of the dielectric function, while the lines represent absorption calculated by FDTD. The excellent match between the two over most of the spectrum indicates the quality of the dispersion model.

stability polynomials in the r-plane [30]. As shown in Fig. 2(c), all the poles in the r-plane are located in the unit circle which means these solutions are unconditionally stable, as is seen in simulation. Using the modeling results, 1-D dispersive FDTD simulations are performed over the wavelengths that we are interested in. Figure. 3 shows that the simulated absorption matches very well to the exact analytical expressions for reflection and transmission applied to literature data for dispersion [35]. Further detailed descriptions of our simulation and validation approach are provided in our previous work [29]. Among the various alloy compositions considered in this work, the RMS errors between simulated absorption and analytical absorption ranged from 0.29 to 0.61%, which is, in fact, substantially lower than the fitting error.

3. Results and discussion

In this section, light trapping structures will be introduced to CZT/Si cells step by step. In order to develop strong intuition as to the nature of absorption enhancement of pyramidal texturing and asymmetric back gratings, we first optimize them in thin-film silicon single junction cells (1.8-μm-thick). Then, the top CZT cells are added to the previously optimized structures. Note that J_{ph} for the top and bottom junctions may not be matched during the first phase of our light trapping studies, but in the second phase, a comprehensive current matching study will consider the effect of various CdTe alloy compositions.

3.1. Pyramidal texturing

It is clear from the literature that the planar thin layers of crystalline silicon are not sufficient to fully absorb sunlight. Thus, in order to fully trap light within thin active layers of c-Si, we consider pyramidal texturing at the front and dielectric gratings at the back. Assuming that photons with energies above the CZT bandgap may not reach the silicon layer, the optical design should focus on energies between the c-Si and CZT bandgaps, corresponding to wavelengths ranging from 700—1100 nm. Note that the maximum short circuit current density (J_{ph}) is

#262116 Received 1 Apr 2016; revised 9 May 2016; accepted 10 May 2016; published 20 May 2016
© 2016 OSA

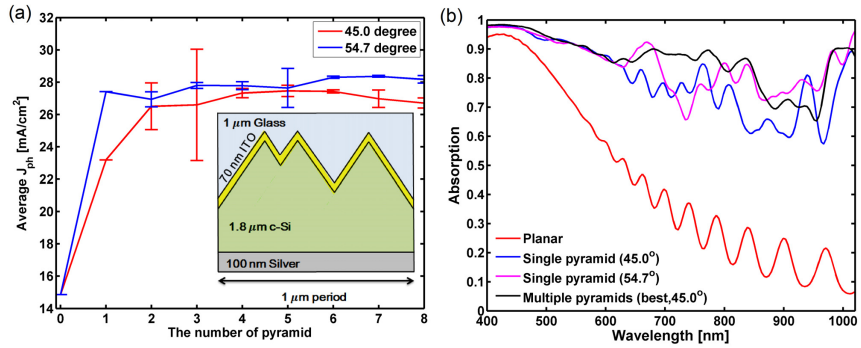

Fig. 4. (a) Average J_{ph} for various number of pyramids in thin-film c-Si cells. J_{ph} for 45.0° pyramids increases for up to two pyramids and then it plateaus while J_{ph} for 54.7° plateaus from the single pyramid case. Standard errors are calculated for 5 simulation trials. The inset figure shows a cross-section of the simulation geometry (b) Absorption spectra for four representative cases.

calculated under an ideal IQE (without charge collection losses), an AM1.5G solar spectrum :

$$\mathrm{J_{ph}} = \int_{300\mathrm{nm}}^{1100\mathrm{nm}} d\lambda \left[\frac{e\lambda}{hc} \frac{dI}{d\lambda} A(\lambda) \right], \tag{1}$$

where the $A(\lambda)$ is a simulated partial absorption for each photovoltaic volume, and $\frac{dI}{d\lambda}$ represents the light intensity experienced by the solar cell per unit wavelength (given by the AM1.5 solar spectrum).

Here, we numerically demonstrate an optimization of the pyramidal front texturing. In the process of fabricating a silicon-based solar cell, 54.7° pyramidal texturing could be achieved using the well-known process of KOH anisotropic etching [36, 37]. It has been shown that pyramidal texturing can enhance light absorption dramatically in thin film silicon solar cells, although not quite at the theoretical maximum [37]. To simplify any potential fabrication of our structures, we constrain ourselves to a fixed periodicity (1 μm) and upright pyramids with two opening angles (i.e., 45.0° and 54.7° which correspond to aspect ratios of 1 and $\sqrt{2}$, respectively).

As shown in Fig. 4(a), a single pyramid offers significant light trapping compared to the planar case for both 45.0° and 54.7°, while the best multiple pyramid cases also show an additional 5.39 mA/cm^2 J_{ph} for 45.0° pyramids and 1.39 mA/cm^2 J_{ph} for 54.7° pyramids compared to the single pyramid case. Note that the location of each pyramid is randomly distributed and simulated, and five simulations have been done for each value of the number of pyramids. The J_{ph} enhancement plateaus after two pyramids for both cases. The absorption curves for the representative cases are shown in Fig. 4(b).

Figures 5(a) and 5(b) show simulated texturing surfaces. Within the condition of a fixed pyramid height (500 nm), the optimized J_{ph} was 28.57 mA/cm^2 when the number of pyramids was three. To validate this result, we applied spatial Fourier transform to these surfaces. As shown in Fig. 5(c) and 5(d), the multiple-pyramid mode has a stronger peak at the central Fourier component, compared the single-pyramid case. FFT analysis can provide the number of modes with appreciable amplitudes, which may give a general sense of the potential for absorption enhancement.

We confine our work to a simple texturing method so that it would be more reproducible in a templated KOH etch-based fabrication process. It only includes two pyramids per period with 45°, one at the center and one at the corner of the computational cell, with a maximum height

#262116 Received 1 Apr 2016; revised 9 May 2016; accepted 10 May 2016; published 20 May 2016
© 2016 OSA

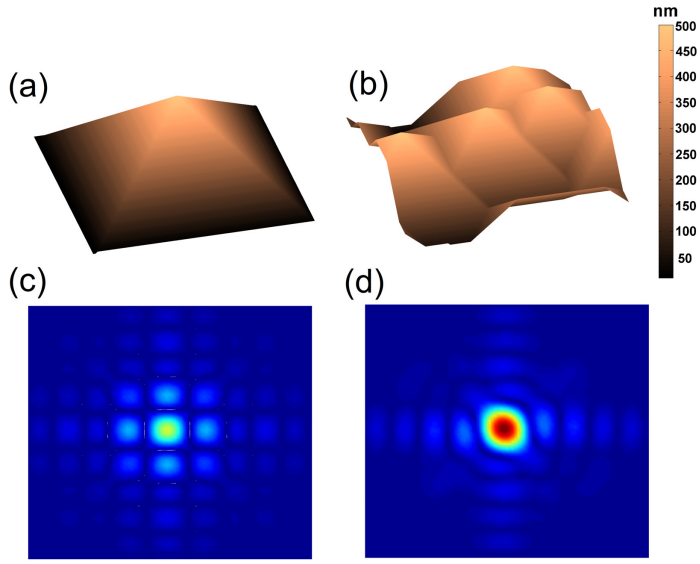

Fig. 5. (a) Single pyramidal surface. (b) The optimum multiple pyramids case. (c) Spatial Fourier transforms of a single pyramid. It shows a broader mode with a smaller center peak. (d) Fourier transform of optimized multiple pyramids. It has the strongest center mode with well-distributed local modes.

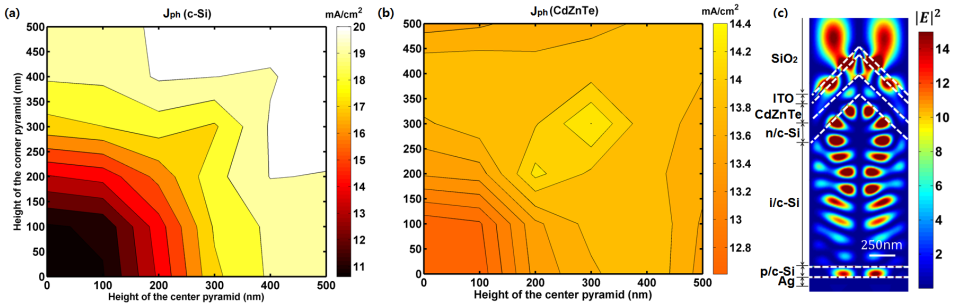

Fig. 6. (a) Contour plot showing J_{ph} of c-Si versus heights of two pyramids ($h1$, $h2$) for front-surface texturing of c-Si within the computational cell. Due to the symmetric design, the optimal performance (J_{ph} = 20.62 mA/cm^2) is predicted when $h1$ = 500 nm and $h2$ = 400 nm or vice versa. Filtering effect by CZT layer lowers c-Si J_{ph} from the single junction J_{ph}. (b) Contour plot showing J_{ph} of CZT versus heights of two pyramids ($h1$, $h2$) (c) 2-D slice of the electric field intensity squared at $\lambda = 1000$ nm for the optimum cell.

#262116 Received 1 Apr 2016; revised 9 May 2016; accepted 10 May 2016; published 20 May 2016
© 2016 OSA

of 500 nm. Now, we apply $Cd_{0.5}Zn_{0.5}Te$ (E_g = 1.81 eV) to the top junction of the tandem cell. The thicknesses of the CZT and c-Si layers are fixed to a total thickness of 2 μm, with layer thicknesses of 200 nm and 1800 nm, respectively. The considerations that went into selecting the optimum bangap of CZT are discussed later. In order to measure the electromagnetic flux transmitted and reflected at the boundary of CZT and c-Si layer, the FFP is inserted at their textured boundary.

Figure. 6 shows that the J_{ph} of c-Si is enhanced quite significantly by increasing the height of each pyramid. Note that the J_{ph} of CZT changes by only about 9.80% while c-Si J_{ph} changes 48.47 %. This is mainly because light trapping is more relevant for indirect bandgap materials, such as c-Si in the bottom cell. The optimum J_{ph} for c-Si of 20.62 mA/cm^2, is observed when h_1 = 500 nm and h_2 = 400 nm, while the corresponding CZT J_{ph} is 13.80 mA/cm^2. The significant J_{ph} mismatch in this result could be adjusted either by increasing the CZT thickness or increasing its cadmium concentration, which will be discussed in the later section. Compared to a J_{ph} for flat c-Si of 10.62 mA/cm^2, this represents a 94.12% enhancement over the flat structure. In the case of CZT, the enhancement of J_{ph} is limited to 9.50%, suggesting this factor can be mostly ignored. Since the positions of the two pyramids are fixed at the center and the corner, respectively, the contour plot shown in Fig. 6 has a symmetrical form.

3.2. *Asymmetric dielectric grating*

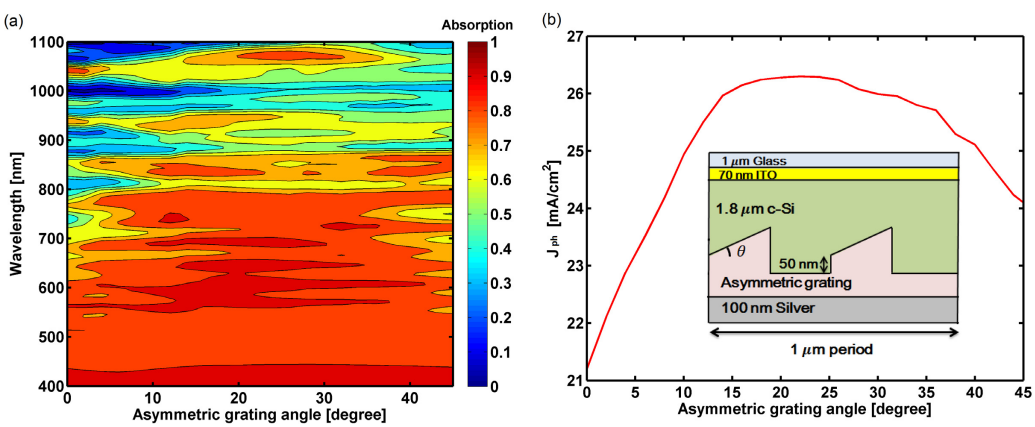

Fig. 7. (a) 3-D FDTD simulation results for various grating asymmetric angles. The maximum angle is restricted to 45° to satisfy an aspect ratio of 1. For higher wavelengths (800 nm–1100 nm), strong absorption modes are observed at 850 nm, 930 nm, 1060 nm. These three modes overlap strongly near the 20° grating angle, resulting in the highest J_{ph}. (b) J_{ph} for various grating angles. It linearly increases with increasing angle and it plateaus up to 25°, and then decreases. The inset shows a 3-D asymmetric grating structure.

To enhance light trapping in c-Si significantly further, we also would like to add a back reflector. Various designs have been suggested for a back reflector, including randomly textured [38], periodic [39], sphere gratings [40] and plasmonic back reflectors [41, 42]. However, metallic grating structures have parasitic absorption associated with an undesired excitation of surface plasmon polaritons (SPPs), propagating at the metal/dielectric interface [43]. Especially in thin film designs, the amount of incoming light reaching the metal back reflector is greater than in the wafer-based solar cell; therefore, the excitation of SPPs could be a significant problem. Thus, we avoid textured metal back reflectors and consider a flat metal back reflector with an asymmetric dielectric grating on top of the metal. In general, dielectric gratings have been calculated to enhance broad-band absorption, without strong parastitic abs-

#262116 Received 1 Apr 2016; revised 9 May 2016; accepted 10 May 2016; published 20 May 2016
© 2016 OSA

orption, without strong parasitic absorption [44]. They can be manufactured at low cost with relatively small series resistance by laser-fired and grooved contacts [45], which include an intermediate dielectric layer. The laser-fired contacting method can overcome several disadvantages of a eutectic metal backing, such as suboptimal reflection at the metal/silicon interface, Schottky barriers due to the work function of metal, and carrier recombination at the silicon-metal interface.

It has been shown that asymmetric dielectric gratings outperform their more typical symmetric counterparts [46]. However, the shapes and angles of asymmetric gratings have not been investigated sufficiently. In this work, we study the angular dependency of asymmetric gratings. 3-D FDTD simulations are performed to find the optimum angle of the grating structure. Note that the refractive index of asymmetric gratings are assumed to be 1.5, for an angular dependent study, and then the refractive index dependency will be studied. The front side of the solar cells is assumed to be flat and the average thickness of absorber layer is conserved. Figure. 7 shows what happens if one starts with a symmetric grating (the zero asymmetric angle case) and then gradually increases the asymmetric angle. Figure. 7(a) shows the absorption spectrum as a function of the asymmetric angle. For higher wavelengths (800nm–1100 nm) which is relevant to c-Si absorption, strong absorption modes are observed at 850 nm, 930 nm, 1060 nm. These three modes overlap strongly near the 20° grating angle, resulting in the highest J_{ph} in Fig. 7(b). The J_{ph} also gradually increases until reaching a plateau after 20°, then it decreases. This roughly corresponds to the critical angle of SiO_2 and c-Si boundary, which is defined by $\theta_c = \sin^{-1}(n_{glass}/n_{si})$, where θ_c is the critical angle of the material boundary, n_{glass} is the refractive index of glass and n_{si} is the refractive index of c-Si. The results clearly show that asymmetric gratings have better light absorption than symmetric dielectric gratings (the zero degree case), as shown in Fig. 7(b).

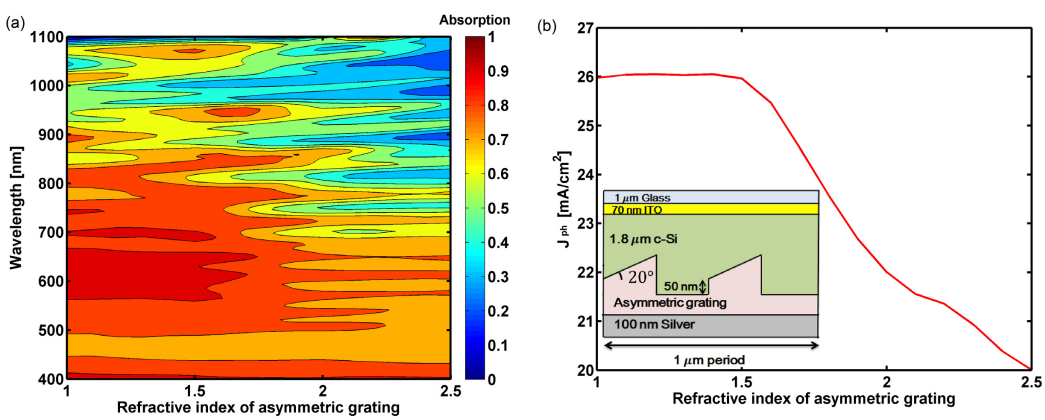

Fig. 8. Refractive index dependency of asymmetric grating. J_{ph} was obtained in a 3-D FDTD simulation with different refractive index of the asymmetric gratings. (a) Absorption spectrum for varying refractive index. (b) J_{ph} for various refractive index. J_{ph} plateaus up to n = 1.5, and then decrease linearly. The inset shows a simulation structure.

Based on the optimum grating angle obtained in this study, we then vary the refractive index of our asymmetric gratings in 3-D FDTD simulations. Figure. 8(a) shows the absorption spectrum with variation in the refractive index. Note that the apparent plateau shown in Fig. 8(b) is a coincidence arising from the integration of multiple absorption peaks over a refractive index range from 1.0 to 1.5. The J_{ph} decreases gradually after the plateau. This is mainly because a large refractive index contrast may offer a better scattering effect at the material boundary. Among several dielectric spacers, SiO_2 may have an optimal performance due to its

#262116 Received 1 Apr 2016; revised 9 May 2016; accepted 10 May 2016; published 20 May 2016
© 2016 OSA

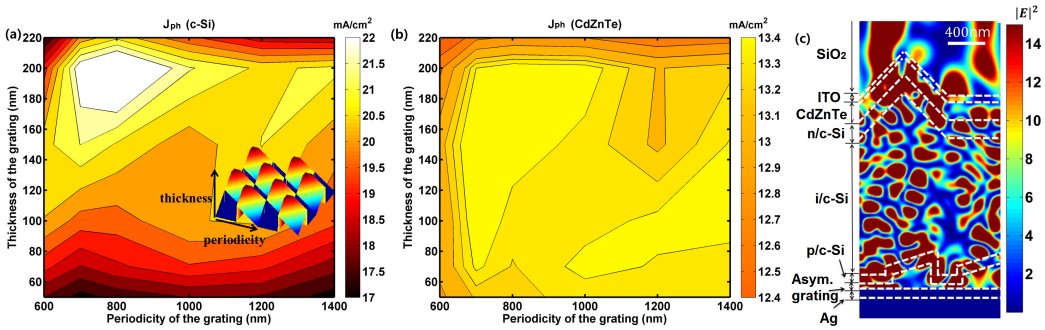

Fig. 9. (a) Contour plot showing J_{ph} of c-Si versus grating thickness (t) and periodicity (p) values (in nm) within the computational cell. Note that the pre-optimized front texturing obtained from Fig. 6 is applied in this optimization. The optimum point (J_{ph} = 23.47 mA/cm^2) is predicted to occur when grating thickness (t) = 200 nm and periodicity (p) = 800 nm. The inset shows the surface of the asymmetric gratings. (b) Contour plot showing J_{ph} of CZT versus grating thickness (t) and periodicity (p) values (in nm). (c) 2-D slice of Electric field intensity at $\lambda = 1000$ nm in the optimum cell. Compared to Fig. 6(b), the dual-side light trapping cell has strongly guided mode.

refractive index. However, electrical parameters are also considered as an important factor for choosing a dielectric spacer. ZnO has good conductivity that provides lower series resistance, but a refractive index of 2.1, which may cause non-optimal light trapping in asymmetric back gratings. Thus, the ideal transparent conductive oxide for asymmetric gratings would have both low refractive index and relatively high conductivity.

Now, the optimized front texturing ($h1$ = 500 nm, $h2$ = 400 nm) with a tandem configuration is now combined with the pre-optimized asymmetric dielectric grating. Dielectric gratings are tilted 20° from the perpendicular direction in all cases and the refractive index is 1.5 for the optimal light trapping. We now consider the impact of back grating periodicity on hybrid dielectric light trapping. For this purpose, two variables (periodicity and the thickness of the grating) are systemically optimized. Note that the front texturing was originally optimized for a period of 1 μm, but now periodicity is varied. We find that the enhancement of J_{ph} varies within 2.4 % when the periodicities are 1000, 1200, 1400 and 1600 nm. Therefore, it is reasonable to assume that the varying periodicity mostly affects J_{ph} enhancement from dielectric gratings in these simulations. Figure. 9 shows that the J_{ph} of the c-Si layer increases to 23.47 mA/cm^2 (h = 200 nm, p = 800 nm), which corresponds to an enhancement of 121 %, compared to the flat structure. As discussed in the previous section, the J_{ph} enhancement of CZT was negligible. Despite this large increase, light trapping alone is not enough to achieve good current matching. This result implies that other design parameters, especially in CZT region, will also need to be adjusted for optimal performance.

3.3. *Current matching for CZT/Si tandem cells*

After showing that J_{ph} can be improved significantly by applying a front texturing and a back grating, here, we suggest a current matching process as follows. First, for a fixed CZT alloy ratio (x = 0.6), we demonstrate a conventional current matching strategy by adjusting a CZT layer thickness. Then, we will allow for simultaneous adjustment of CZT layer thickness and CZT alloy ratios. Figure 10 shows 3-D FDTD simulation results for the $Cd_{0.6}Zn_{0.4}Te$ alloy based tandem cells. CZT J_{ph} is highly dependent on CZT thickness, while c-Si J_{ph} is affected by both light trapping and CZT thickness. In Fig. 10(c), the optimum J_{ph} is 18.21 mA/cm^2 when the

#262116 Received 1 Apr 2016; revised 9 May 2016; accepted 10 May 2016; published 20 May 2016
© 2016 OSA

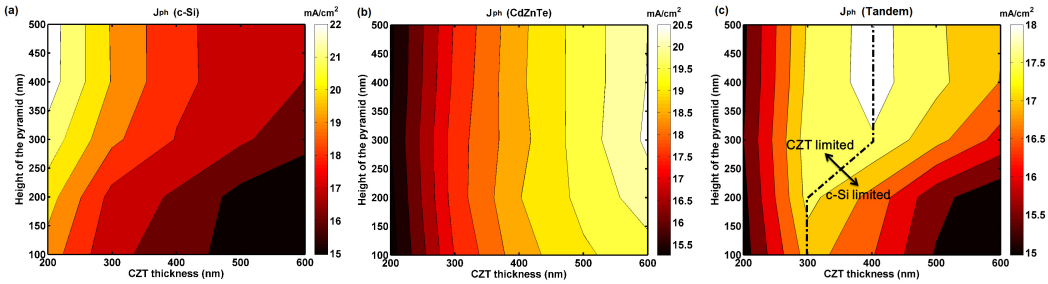

Fig. 10. (a) Contour plot showing J_{ph} of c-Si versus height of pyramid and CZT thickness. (b) Contour plot showing J_{ph} of $Cd_{0.6}Zn_{0.4}Te$ versus height of pyramid and $Cd_{0.6}Zn_{0.4}Te$ thickness. (c) The matched current density. The dashed line indicates the current-matching condition.

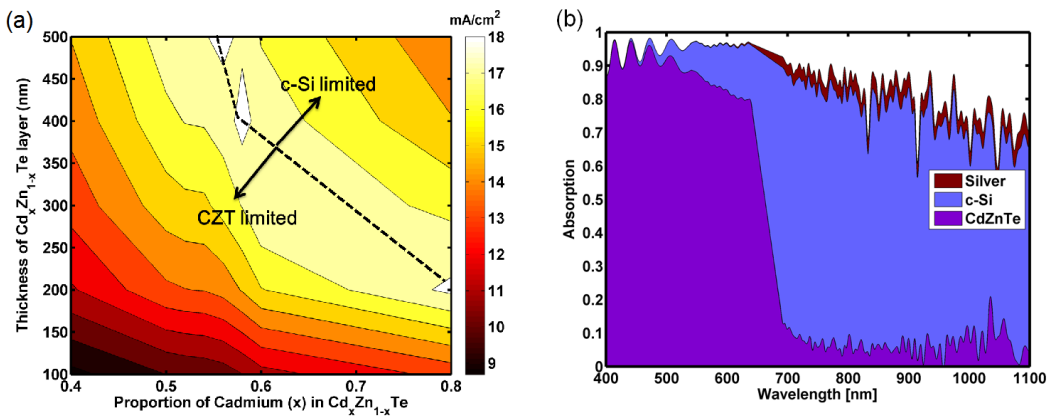

Fig. 11. (a) Contour plot showing the matched J_{ph} of the tandem cell versus both thickness of $Cd_xZn_{1-x}Te$ layer and proportion of Cadmium (x). The maximum J_{ph} is 18.37 mA/cm^2 when x = 0.58 and CZT thickness = 400 nm. (b) Partial absorption for the optimum point found in (a).

CZT layer has 400 nm thickness and the height of pyramid is 500 nm. Again, the filtering effect by CZT layer lowers the c-Si J_{ph} from the single junction optimum J_{ph}. We expect that front pyramidal texturing that exceeds aspect ratio of 0.5 may increase c-Si J_{ph} slightly, causing the matched current condition (dashed line in Fig. 10(c)) to be shifted in the right direction.

Now, we consider CZT alloys with cadmium fractions x ranging from 0.4 to 0.8; we assume that the CZT alloys has different dielectric dispersion depending on their bandgap. We then increase the thickness of $Cd_xZn_{(1-x)}Te$ slightly up to 500 nm to match the current flow at each junction. The optical simulations are performed with various CZT alloys via QCRF-FDTD method incorporated with the proposed material models; the resulting fractional absorption spectrum is then used to calculate J_{ph} for each junction.

As shown in Fig. 11(a), the matched J_{ph} is sensitive to both the thickness of CZT and proportion of cadmium. Note that after the thickness of CZT reaches 400 nm, J_{ph} does not change much, resulting in a plateau in the contour plot. In Fig. 11(a), the maximum J_{ph}, 18.37 mA/cm^2, occurs when $x = 0.58$ and $h = 400$ nm. It is shown that in thin-film tandem cells, current matching can be achieved by adjusting both bandgap and thickness of CZT, while wafer based tandem cells utilizes the bandgap only. Figure 11(b) shows that using ultra-thin crystalline silicon does entail a slight reduction in overall absorption even in the presence of

#262116 Received 1 Apr 2016; revised 9 May 2016; accepted 10 May 2016; published 20 May 2016
© 2016 OSA

experimentally-relevant light trapping structures, as discussed previously. The corresponding maximum efficiency is predicted to be 16.08 % using the most conservative interpretation of the electrical parameters measured in experiment [9]. Using the same electrical parameters as used for the CZT/c-Si tandem, we find that the 2.2-μm-thick c-Si thin film with the same hybrid light trapping scheme has an efficiency of 12.79 %. Thus, the tandem offers a relative performance improvement of 25.72 %. We also compared the hybrid light trapping scheme with state of the art thin-film c-Si cells (e.g., a 7.3 % efficient a plasmonic cell [42], a 9.0 % efficient random texturing cell [47], and a 10.7 % efficient periodic texturing cell [48]). Even though our structure includes a thick glass layer causing nearly 4 % Fresnel reflection at the air/glass interface, it shows improved absorption compared to the referenced cells. Improved CZT material quality (e.g., single crystal growth) could also improve performance, but that is a non-trivial challenge that goes beyond the scope of this investigation of low-cost thin-film growth.

4. Conclusion

In this work, we investigated a thin-film tandem solar cell structure utilizing II-VI wide-bandgap alloys on top of crystalline silicon solar cell, which theoretically can have 42 % [3] cell efficiency with one sun illumination using the corresponding bandgaps, greatly exceeding the single-junction S-Q limit. In the interest of achieving high-performance CZT/Si ultra thin film designs, novel optical simulation methods were proposed and verified with theoretical analysis and experimental data. An optimized pyramidal texturing and dielectric back gratings are both shown to greatly enhance the average path length of incident photons for a thin-film tandem cell significantly. As a result, J_{ph} in the silicon layer is increased by 120.99 % from the flat structure after adding both of these light-trapping features. Our optical simulations predict that 2.2 μm (0.4 μm CZT, 1.8 μm c-Si) thin-film cells can have matched J_{ph} = 18.37 mA/cm^2. In short, the thin-film CZT/Si material system combined with the proposed hybrid light trapping scheme shows that there is great potential for high-performance, low-cost tandem cells to approach or exceed the S-Q limit.

Acknowledgments

The authors thank Xufeng Wang and Mohammad Ryyan Khan for valuable discussions. Support was provided by the Department of Energy, under DOE Cooperative Agreement No. DE-EE0004946 (PVMI Bay Area PV Consortium) and the Basic Research Program through National Research Foundation of Korea (NRF) funded by the Ministry of Education (No. 2014R1A1A205440).

#262116 Received 1 Apr 2016; revised 9 May 2016; accepted 10 May 2016; published 20 May 2016
© 2016 OSA